Materials Research Proceedings 54 (2025) 199-208 https://doi.org/10.21741/9781644903599-22

Porosity analysis of L-PBF manufactured AZ91D components

Lennart Grüger[1,a *], Joanna Szyndler[1,b], Felix Jensch[1,c] and Sebastian Härtel[1,d]

[1]Department Hybride Manufacturing BTU Cottbus Senftenberg, Konrad-Wachsmann-Allee 17, 03046 Cottbus, Germany

[a]Lennart.Grueger@b-tu.de, [b]Joanna.Szyndler@b-tu.de, [c]Felix.Jensch@b-tu.de, [d]Sebastian.Haertel@b-tu.de

Keywords: AZ91D, Additive Manufacturing, L-PBF, HIP, Process Parameter Analysis

Abstract. Several materials for joint replacement parts approved in medical technology are being investigated. Magnesium alloys are very suitable for implants due to the similar strength properties between magnesium alloys and human bone. Therefore, the present work aims to examine the parameters for producing the magnesium alloy AZ91D. For this purpose, 16 samples were manufactured with varying laser power and exposure speed and examined using µCT analyses. As a result, densities between 99.56 and 95.21 percent were achieved. The samples with the lowest density were subjected to a HIP process to increase the relative density. However, a further µCT analysis revealed only minor positive effects of the HIP process. An analysis of the number and size of the pores indicates that the pores bonded together instead of being closed.

Introduction

Various materials approved for use in medical technology are currently being investigated for joint replacement parts. Due to the similar strength properties between magnesium alloys and human bone (see Fig. 1), magnesium alloys are highly suitable for implants [1].

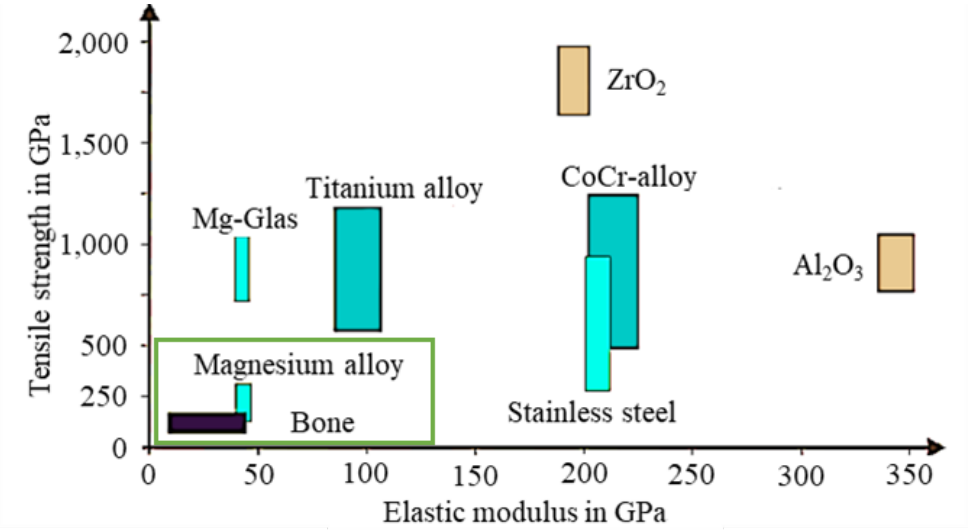

Figure 1 – Overview of the material properties of metallic materials in medical technology compared to human bone according to [1].

In addition, magnesium degrades independently in the body. It does not need to be surgically removed after healing, making it ideal for use in temporary implantation scenarios such as bone fixation devices [2-6]. Since the production of magnesium implants using the L-PBF process has only been researched more intensively since the mid-2010s, there is less experience with its production than with titanium alloys. Wu et al., Savalani et al., and Ng et al. have investigated the manufactured components' process parameters and the resulting density and corrosion resistance

[2-4]. Promising investigations with lattice structures were also carried out for magnesium alloys to further approximate the mechanical properties between implant and bone and the connection to the body [5]. In a comparative study, Matena et al. have shown that coated magnesium implants are just as promising as the already widely used titanium implants [6]. The work of Liu et. al, Tsakiris et al. Vignesh et al., Kaushik et al., Yue et al., and Manakari et al. provide an overview of the current applications, challenges, and opportunities of additively manufactured magnesium components in medical technology [7-12].

L-PBF parameter studies have also been performed for magnesium alloys in the past. Sharma et al. give an overview of some of the results. Based on the summary, Table 1 shows the different parameters and the relative densities generated for the material AZ91D [13].

Table 1 – An overview of selected parameter studies on the material AZ91D according to [13]

Size and Shape of Powder	Parameter					Energy Density [J/mm³]	Relative Density [%])	Reference
	Power [W]	Spot Size [µm]	Speed [mm/s]	Layer Thickness [µm]	Hatch Spacing [µm]			
59 µm, spherical	200		333	40	90	167	99,52	[14]
53–75 µm, spherical	130	80	10	350	500	74	95,9	[15]
30 µm, spherical	50		200	30	30	278	98,1	[16]

Wei et al. varied the scanning speed between 167 and 1000 mm/s and the hatching distance between 70 and 130 µm at constant layer thickness (40 µm) and laser energy (200 W). Using a hatching distance of 90 µm and a layer thickness of 40 µm, they achieved a relative density of 99.52 % [14]. Zhu et al. varied the laser power between 80 and 130 W and the hatching distance between 500 and 1500 µm. They achieved a relative density of 95.9 % at a power of 130 W and a hatching distance of 500 µm [15]. Niu et al. varied the scanning speed between 200 and 500 mm/s to adjust the energy density. The highest relative density of 98.1 % was obtained at the lowest scanning speed [16]. The compared tests show that, despite widely differing energy inputs, similar relative densities can be achieved depending on the powder size and parameter settings.

Due to the described advantages of using the AZ91D alloy for implants [1] and the possibility of manufacturing bone-like structures using L-PBF [11], the authors aim to determine suitable parameters for producing AZ91D geometries with L-PBF. The literature reports positive effects on the improvement of mechanical properties such as the elongation or ultimate tensile strength and a possible reduction of porosity [17-19]. However, there are also reports that document no positive effect of the HIP process at a high near-surface porosity [20].

Materials and Methods

Materials. The press-on sleeves were manufactured from AZ91D magnesium alloy powder supplied by Hana AMT Co Ltd. The sleeves measure 30 mm in outer diameter, 5 mm in wall thickness and 9 mm in height, as shown in Fig. 2. The particle size of the powder was between 20 and 63 µm. The chemical composition of the powder can be found in Table 2, according to the manufacturer's specifications.

Table 2 – Chemical composition of the AZ91D powder in wt.%

Material	Mg	Al	V	Fe	Zn	Mn
AZ91D	bal	8.00	-	0.009	0.97	0.2

Methods. Manufacturing of Samples. The AconityMIDI equipment was used for sample manufacturing, which has a laser with a focus diameter of 80 µm and a wavelength of 1070 nm. All 16 samples were produced in an argon atmosphere with a layer thickness of 30 µm and a hatching distance of 60 µm. The varied process parameters and the sample geometry are shown in Fig. 2.

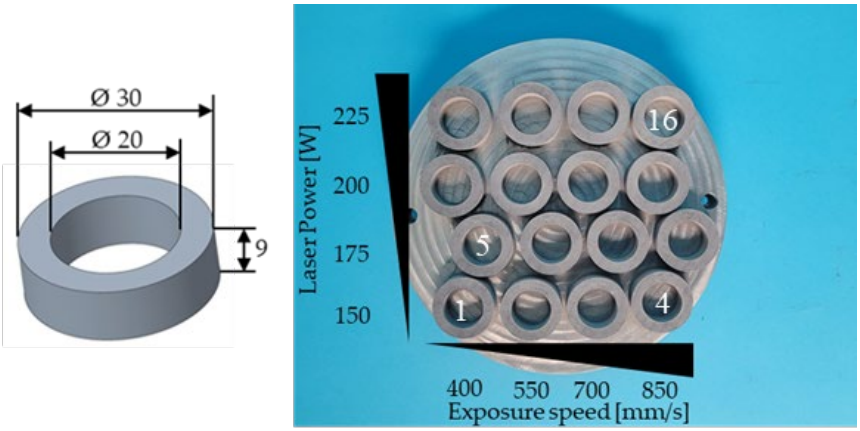

Figure 2 – Visualization of the Sample geometry (left) and production result, as well as production parameters (right).

µCT Analysis. The defect analysis was performed using computed tomography (µCT). For this purpose, a CoreTOM µCT from TESCAN was used. An aluminum (Al) filter with a thickness of 1 mm was used to provide the required X-ray energy and reduce radiation hardening. The entire test setup is shown in Fig. 3.

Figure 3 – Visualization of the experimental setup of the µCT analyses

Due to the applied scan parameters, the minimum detectable pore size was ≈17,65 µm. Similar values are given in [21]. The entire sample was scanned and analyzed, excluding the top and bottom layers. The pore analysis was performed using VGSTUDIO MAX (V2022.1) software from Volume Graphics. An overview of the scan parameters is shown below:

- Energy: 80 kV,

- Power: 15 W,
- Detector: HW1, SW1, HIGH,
- Exposure Time: 2500 ms.

Hot isostatic pressing. After the first µCT scans, selected samples were post-processed using HIP. For this purpose, a HIP process was carried out on a Quintus QIH 15L using the following parameters:

- Temperature: 490 °C,
- Time: 3 h,
- Pressure: 100 MPa,
- Shield gas: Argon.

Results

The micro CT results shown in Fig. 4 demonstrate that the defect volume ratio decreases with proportionality to the scanning speed and laser powers, as assumed. The lowest defect volume rate of 0.44 % is determined at a scanning speed of 550 mm/s and a laser power of 150 W. The highest defect volume rate of 4.79 % is detected at a scanning speed of 850 mm/s and a laser power of 175 W. Regardless of the energy density applied, the defect volume ratio is always highest at this scanning speed. These are between 4.79 % and 4.55 %, with energy densities between around 98 J/mm³ and around 131 J/mm³. Furthermore, the optimum of the examination with a defect volume rate of 0.44 % is found at an energy density of around 152 J/mm³ with a laser power of 150 W and a scanning speed of 550 mm/s. However, the fifth worst result in the study is achieved at a similar energy density of 158 J/mm³, resulting from a laser power of 200 W and a scanning speed of 700 mm/s, with a defect volume ratio of 4.53 %.

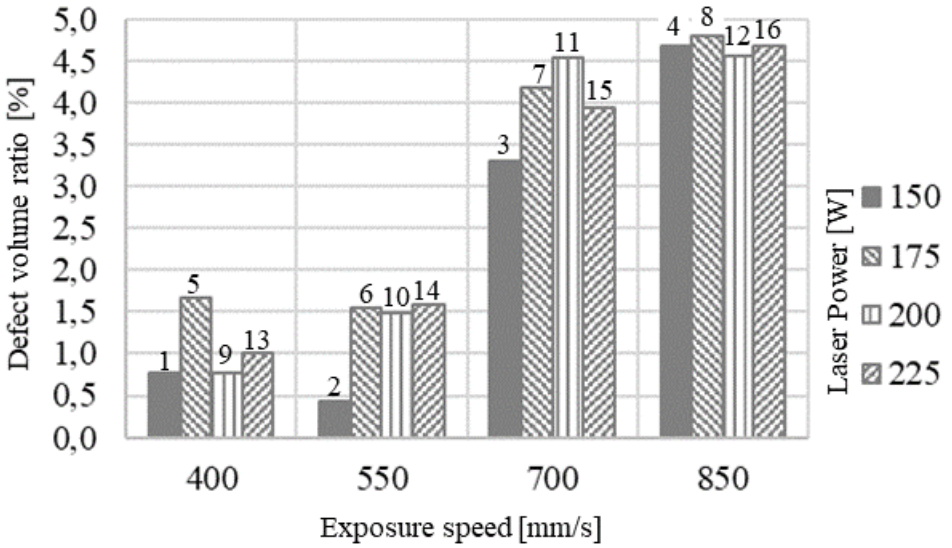

Figure 4 – Visualization of the defect volume ratio according to exposure speed and laser power

The three samples with the highest defect rate (no. 4, 8, 16) were subjected to hot isostatic pressing with the parameters mentioned in chapter hot isostatic pressing. These were then re-analyzed by µCT. Table 3 compares the absolute defect volume ratio before and after heat treatment.

Table 3 – Comparison of the defect volume ratio before and after heat treatment.

Sample number	defect volume ratio before HIP [%]	defect volume ratio after HIP [%]	Decrease [%]
4	4.67	4.3	7.92
8	4.79	4.64	3.13
16	4.67	4.51	3.43

When examining the change in defect volume ratio, the results show that this decreases by 7.92 % in sample 4 and 3.13 % in sample 8. Accordingly, the relative densities change only marginally from 95.33 % to 95.7 % in sample 4 and from 95.21 % to 95.63 % in sample 8.
Further analysis of the µ-CT results enabled Authors to investigate the possible causes more precisely. Table 4 shows the total number of pores before and after the HIP process and the equivalent diameter of the most significant pore of each sample.

Table 4 – Comparison between the number of pores before and after HIP.

Sample number	Total number of pores before HIP	Total number of pores after HIP	Decrease [%]	Equivalent diameter of the largest pore before HIP µm	Equivalent diameter of the largest pore, after HIP µm
4	327,893	297,050	9.4	710.26	611.16
8	399,981	304,186	23.94	567.89	607.72
16	349,179	297,621	14.76	681.37	636.94

The first analysis shows that the largest relative reduction in the number of pores, at around 24 %, is found in sample 8. However, this sample shows the lowest decrease in the defect volume ratio with 3.13 %. Furthermore, the equivalent diameter of the biggest pore, after HIP in sample 8, increases from around 570 µm to 608 µm in contrast to the other samples. Sample 16 suggests a similar analysis in an attenuated form. Here, too, the number of pores decreases by about 15 percent, while the defect volume ratio decreases by only 3.43 percent. Although the equivalent diameter of the biggest pore does not increase in sample 16, the assumption is made that the pores merge and are not closed. This assumption was investigated by further processing the data from the µ-CT analysis. Fig. 5 shows the number of pores and the equivalent pore size before and after the HIP process.

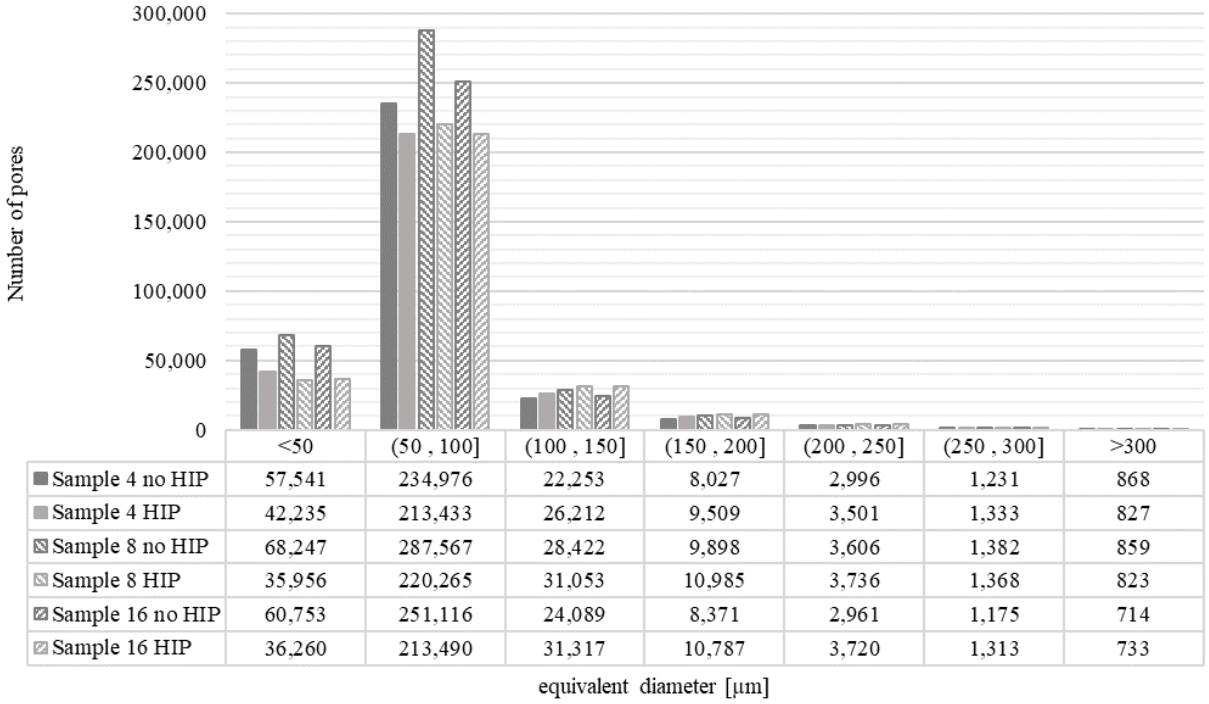

	<50	(50 , 100]	(100 , 150]	(150 , 200]	(200 , 250]	(250 , 300]	>300
Sample 4 no HIP	57,541	234,976	22,253	8,027	2,996	1,231	868
Sample 4 HIP	42,235	213,433	26,212	9,509	3,501	1,333	827
Sample 8 no HIP	68,247	287,567	28,422	9,898	3,606	1,382	859
Sample 8 HIP	35,956	220,265	31,053	10,985	3,736	1,368	823
Sample 16 no HIP	60,753	251,116	24,089	8,371	2,961	1,175	714
Sample 16 HIP	36,260	213,490	31,317	10,787	3,720	1,313	733

Figure 5 – Visualization of change in a number of pores in subsequent ranges of their equivalent diameter in samples no. 4, 8, and 16.

The analysis of the processed data supports the assumption that the pores merge instead of being closed. Thus, the number of pores up to 100 µm equivalent diameter decreases in all samples. The number of pores in sample 8 decreases by 47.31 % for an equivalent diameter up to 50 µm and 23.4 % between 50 and 100 µm. In sample 16, the number of pores decreases by 40.32 % up to 50 µm and around 15 % between 50 and 100 µm equivalent diameter. Table 5 shows the reduction in the number of pores in the respective equivalent diameter range in percent.

Table 5 – Change of the number of pores for each equivalent pore diameter range in percent.

	Change of the number of pores after HIP [%]		
Range \ Sample no.	Sample 4	Sample 8	Sample 16
<50	-26.60	-47.31	-40.32
(50, 100]	-9.17	-23.40	-14.98
(100, 150]	17.79	9.26	30.01
(150, 200]	18.46	10.98	28.86
(200, 250]	16.86	3.61	25.63
(250, 300]	8.29	-1.01	11.74
>300	-4.72	-4.19	2.66

The results show that the number of pores after HIP decreases for the range below 100 µm but increases for an equivalent diameter of over 100 µm in almost all analyzed value ranges. In order to investigate the fact that the HIP process could have no positive effect on a possible near-surface porosity as a possible cause, a cross-section of the µ-CT analyses before and after HIP was examined. The comparison of samples 4, 8 is shown in Fig. 6. These show the greatest (7.92% for sample 4) and lowest (3.13% for sample 8) decrease in defect volume ratio.

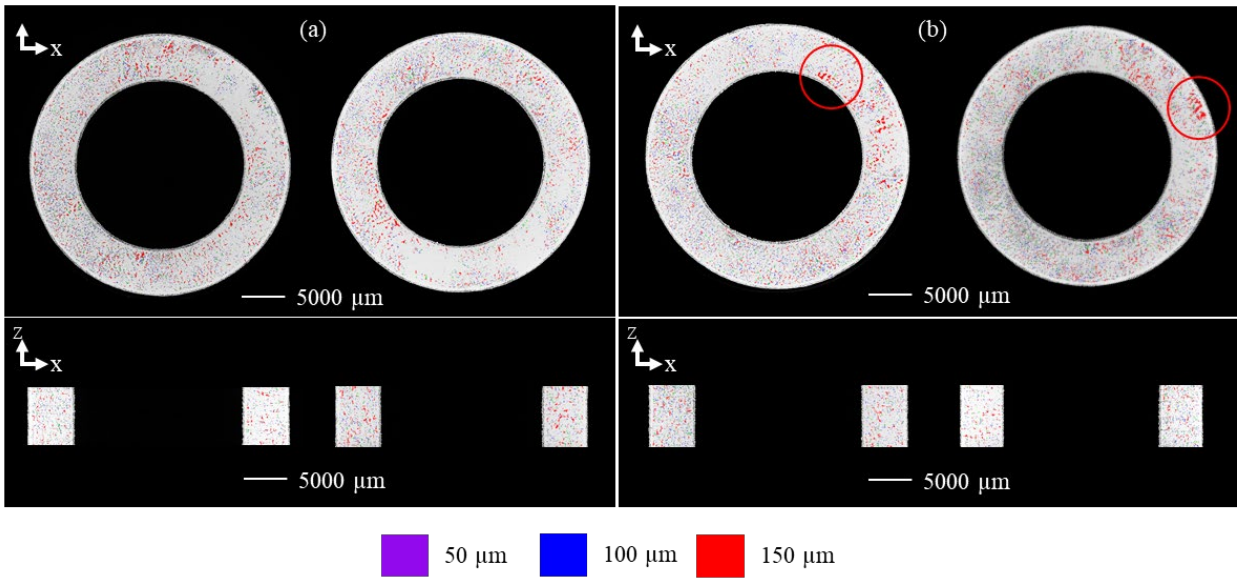

Figure 6 – Cross-section of the µCT analyses of sample 4 (a) and sample 8 (b) before left and after HIP (right)

The visual examination of the sectional images for sample 4 shows an almost equal distribution of the pores in the sample, and the reduction in the defect volume ratio is also visible. In sample 8, on the other hand, pores near the surface are clearly visible on the inner right-hand side even before HIP. After HIP, there is also a concentration of pores with an equivalent diameter of 150 µm near the upper right surface. Nevertheless, the pores in sample 8 are essentially equally distributed throughout the sample.

Discussion

The parameter study carried out as part of the work varied the laser power between 150 and 225 W and the exposure speed between 400 and 850 mm/s. The lowest defect volume rate of 0.44 % is determined at a scanning speed of 550 mm/s and a laser power of 150 watts.

The defect volume ratio is mostly independent of the energy density used. Both the best result (0.44 % defect volume ratio at around 152 J/mm³) and the worst result (4.79 % defect volume ratio at around 114 J/mm³) are within a process window of between 98 J/mm³ and 158 J/mm³. This contradicts the assumption of [14] that there is a good process window at an energy density of 83 J/mm³ to 167 J/mm³ regardless of considering the individual parameters such as scanning speed and laser power. Moreover, this finding supports the work of [16], in which a higher number of lack-of-fusion pores is detected at a similar energy density and higher scanning speed.

The samples with the highest porosity (4, 8 & 12) were subjected to a HIP process. Further µCT analysis showed that the defect volume ratio decreased between 8. and 3.4 percent, and the defect volume ratio in the samples was still relatively high at 4.64 to 4.3 percent. An analysis of the number compared to the pore size suggested that the pores had bonded rather than being pressed out of the samples. This conclusion is based on the fact that the number of pores below 100 µm decreases in all samples but almost always increases in areas above 100 µm. In [20], it was determined that the HIP process has little to no influence on the density, especially with near-surface porosity. The investigation of the pore distribution shows a result that indicates a tendency of the pores in sample 8 towards the surface. The present pores are essentially equally distributed.

Nevertheless, the increase in porosity after heat treatment is known for additively manufactured AlSi10Mg and can according to the literature be correlated with the amount of trapped gas, mainly hydrogen, and pore coalescence. On the one hand, the abrupt and significant increase in hydrogen solubility is worth mentioning when Al passes into the liquid phase. Due to

the high cooling rates resulting from the AM process engineering specifications, hydrogen, which may be present in the atmosphere of the process chamber or as an impurity in the raw material (spherical powder), can be trapped in the samples. As a result, the trapped hydrogen can migrate, fuse and increase porosity depending on the processing conditions and post-processing heat treatments [22]. Accordingly, there are other studies that report a negative influence of heat treatment on porosity [23, 24]. In addition, there are studies which have established that a HIP process has no positive effect on shrinkage porosity for cast magnesium alloys [19].

Conclusion

The L-PBF manufacturing of the body-compatible magnesium alloy AZ91D was examined within this article. For this purpose, a parameter study was carried out. The laser power varied between 150 and 225 W, and the exposure speed was between 400 and 850 mm/s for production with the AconitiyMIDI. Subsequently, µCt analyses were carried out, which showed that relative densities in a range of 99.56 to 95.21 percent could be achieved. The highest densities were achieved with a laser power of 150 W, an exposure speed of 550 mm/s (99.56 %), and an exposure speed of 400 mm/s (99.23 %) under identical conditions. The samples with the highest porosity were obtained at the highest exposure speed, depending on the laser power. Accordingly, it can be concluded the exposure speed is the main influencing factor, followed by the laser power.

Using a HIP process on the samples with the highest porosity only had a small positive effect on the relative density. Thus, the number of pores with an equivalent pore diameter of up to 100 µm decreased by more than 47 %. However, the number of pores in the size range from 100 to 150 µm increased by up to 30 % simultaneously. Analyzing the number and size of pores in conjunction with the literature, it can be concluded that small pores have joined together, significantly reducing their number, but the number of pores with a diameter greater than 100 µm has increased.

In conclusion, a parameter set could be determined which achieves a high relative density of 99.56 %. Future investigations should aim to gain further knowledge about the influence of the HIP process and to further optimize the process parameters with regard to process speed.

References

[1] N. G. Grün, N. Donohue, P. Holweg, und A.-M. Weinberg, „Resorbierbare Implantate in der Unfallchirurgie“, *J. Miner. Stoffwechs. Muskuloskelet. Erkrank.*, Bd. 25, Nr. 3, S. 82–89, Okt. 2018. https://doi.org/10.1007/s41970-018-0041-6

[2] C. L. Wu, W. Zai, und H. C. Man, „Additive manufacturing of ZK60 magnesium alloy by selective laser melting: Parameter optimization, microstructure and biodegradability“, *Materials Today Communications*, Bd. 26, S. 101922, März 2021. https://doi.org/10.1016/j.mtcomm.2020.101922

[3] M. M. Savalani und J. M. Pizarro, „Effect of preheat and layer thickness on selective laser melting (SLM) of magnesium“, *Rapid Prototyping Journal*, Bd. 22, Nr. 1, S. 115–122, Jan. 2016. https://doi.org/10.1108/RPJ-07-2013-0076

[4] C. Chung Ng, M. Savalani, und H. Chung Man, „Fabrication of magnesium using selective laser melting technique“, *Rapid Prototyping Journal*, Bd. 17, Nr. 6, S. 479–490, Okt. 2011. https://doi.org/10.1108/13552541111184206

[5] K. Xie *u. a.*, „Additively manufactured biodegradable porous magnesium implants for elimination of implant-related infections: An in vitro and in vivo study“, *Bioactive Materials*, Bd. 8, S. 140–152, Feb. 2022. https://doi.org/10.1016/j.bioactmat.2021.06.032

[6] J. Matena *u. a.*, „Comparison of Selective Laser Melted Titanium and Magnesium Implants Coated with PCL“, *IJMS*, Bd. 16, Nr. 12, S. 13287–13301, Juni 2015. https://doi.org/10.3390/ijms160613287

[7] C. Liu, Z. Ren, Y. Xu, S. Pang, X. Zhao, und Y. Zhao, „Biodegradable Magnesium Alloys Developed as Bone Repair Materials: A Review“.

[8] V. Tsakiris, C. Tardei, und F. M. Clicinschi, „Biodegradable Mg alloys for orthopedic implants – A review“, *Journal of Magnesium and Alloys*, Bd. 9, Nr. 6, S. 1884–1905, Nov. 2021. https://doi.org/10.1016/j.jma.2021.06.024

[9] M. Vignesh *u. a.*, „Development of Biomedical Implants through Additive Manufacturing: A Review“, *J. of Materi Eng and Perform*, Bd. 30, Nr. 7, S. 4735–4744, Juli 2021. https://doi.org/10.1007/s11665-021-05578-7

[10] V. Kaushik, N. Kumar B, S. Kumar S, und V. M, „Magnesium role in additive manufacturing of biomedical implants – Challenges and opportunities“, *Additive Manufacturing*, Bd. 55, S. 102802, Juli 2022. https://doi.org/10.1016/j.addma.2022.102802

[11] X. Yue, J. Shang, M. Zhang, B. Hur, und X. Ma, „Additive manufacturing of high porosity magnesium scaffolds with lattice structure and random structure“, *Materials Science and Engineering: A*, Bd. 859, S. 144167, Nov. 2022. https://doi.org/10.1016/j.msea.2022.144167

[12] V. Manakari, G. Parande, und M. Gupta, „Selective Laser Melting of Magnesium and Magnesium Alloy Powders: A Review“, *Metals*, Bd. 7, Nr. 1, S. 2, Dez. 2016. https://doi.org/10.3390/met7010002

[13] S. K. Sharma *u. a.*, „Advancements in the Additive Manufacturing of Magnesium and Aluminum Alloys through Laser-Based Approach“, 2022.

[14] K. Wei, M. Gao, Z. Wang, und X. Zeng, „Effect of energy input on formability, microstructure and mechanical properties of selective laser melted AZ91D magnesium alloy“, *Materials Science and Engineering: A*, Bd. 611, S. 212–222, Aug. 2014. https://doi.org/10.1016/j.msea.2014.05.092

[15] Z. Zhu, M. Zhang, und C. Chen, „Effect of selective laser melting on microstructure and properties of AZ91D alloy“, *Materialwissenschaft Werkst*, Bd. 50, Nr. 12, S. 1484–1494, Dez. 2019. https://doi.org/10.1002/mawe.201800161

[16] X. Niu, H. Shen, J. Fu, und J. Feng, „Effective control of microstructure evolution in AZ91D magnesium alloy by SiC nanoparticles in laser powder-bed fusion“, 2021.

[17] S. Liu und H. Guo, „Influence of hot isostatic pressing (HIP) on mechanical properties of magnesium alloy produced by selective laser melting (SLM)“, *Materials Letters*, Bd. 265, S. 127463, Apr. 2020. https://doi.org/10.1016/j.matlet.2020.127463

[18] W. Zhang, Z. Wei, und H. Xu, „Effect of hot isostatic pressing on the microstructure and properties of magnesium silicide–silicon carbide/aluminum alloy (AlSi7Cu2Mg) composites“, *Adv Compos Hybrid Mater*, Bd. 5, Nr. 3, S. 2611–2619, Sep. 2022. https://doi.org/10.1007/s42114-022-00461-y

[19] B. Zhou, D. Wu, Y. Ding, und R. S. Chen, „The Potential Application of Hot Isostatic Pressing for Magnesium Alloys to Reduce Shrinkage Porosity“, *Inter Metalcast*, Bd. 17, Nr. 1, S. 447–454, Jan. 2023. https://doi.org/10.1007/s40962-022-00785-x

[20] A. Du Plessis und E. Macdonald, „Hot isostatic pressing in metal additive manufacturing: X-ray tomography reveals details of pore closure“, *Additive Manufacturing*, Bd. 34, S. 101191, Aug. 2020. https://doi.org/10.1016/j.addma.2020.101191

[21] N. O. Larrosa *u. a.*, „Linking microstructure and processing defects to mechanical properties of selectively laser melted AlSi10Mg alloy“, *Theoretical and Applied Fracture Mechanics*, Bd. 98, S. 123–133, Dez. 2018. https://doi.org/10.1016/j.tafmec.2018.09.011

[22] L. Girelli *u. a.*, „Evaluation of the impact behaviour of AlSi10Mg alloy produced using laser additive manufacturing“, *Materials Science and Engineering: A*, Bd. 748, S. 38–51, Jan. 2019. https://doi.org/10.1016/j.msea.2019.01.078

[23] L. C. Araújo *u. a.*, „Effects of build orientation and heat treatments on the tensile and fracture toughness properties of additively manufactured AlSi10Mg“, *International Journal of Mechanical Sciences*, Bd. 213, S. 106868, Jan. 2022. https://doi.org/10.1016/j.ijmecsci.2021.106868

[24] L. Wang, S. Wang, und J. Wu, „Experimental investigation on densification behavior and surface roughness of AlSi10Mg powders produced by selective laser melting“, *Optics & Laser Technology*, Bd. 96, S. 88–96, Nov. 2017. https://doi.org/10.1016/j.optlastec.2017.05.006